Supplementary Information:
A systematic analysis of Cu-based membrane-electrode assemblies for CO_2 reduction through multiphysics simulation

Lien-Chun Weng,[1,2] Alexis T. Bell,*[1,2] and Adam Z. Weber*[1]

[1]Joint Center for Artificial Photosynthesis, LBNL, Berkeley CA 94720

[2]Dept. Chemical and Biomolecular Engineering, UC Berkeley, Berkeley CA 94720

Rate parameters determined from aqueous electrolyte systems

Kinetic parameters were extracted from experimental data reported by Ebaid et al, where they measured CO_2R on roughened Cu in $CsHCO_3$.[1] Mass transport effects were deconvoluted through simulation of the boundary layer, estimated to be 80 µm.[2] Species molar balance (Equation 17) and Nernst-Planck (Equation 23) were used to solve for the local pH and CO_2 concentration. The exchange current densities were then obtained through fitting the concentration-dependent Tafel equation (Equation 10) to the experimentally measured partial current densities. The reaction orders with respect to CO_2 concentration were approximated from data reported by Wang et al;[3] the reaction orders with respect to water activity were approximated by considering the number of elementary steps that involve water before obtaining an intermediate with the corresponding number of carbon atoms. This method makes the following assumptions: (1) the surface coverage of intermediates are low such that the fraction of empty sites can be approximated as one; (2) the elementary steps listed in **Table S1** are at quasi-equilibrium.

To obtain the activation energy, we assume an Arrhenius dependence for the exchange current density,

$$i_{o,k} = n_k e A_0 \exp\left(-\frac{E_{a,k}}{RT}\right) \quad (1)$$

where n_k is number of electrons transferred in reaction k, e is the electron charge, and $E_{a,k}$ is the activation energy. We assume a constant preexponential factor, $A_0 = 10^{15}\ s^{-1}$, for all cathodic reactions, and back calculate $E_{a,k}$ from the exchange current density. The activation energies are listed in **Table S1**. **Figure S1** shows how the simulated partial current densities for the aqueous system compare to experimental data.

Table S1 Estimated activation energy, the Peltier coefficient, and reaction order with respect to a_w

Product	E_a (kJ/mol)	Π_k (mV)	Elementary steps involving water	γ_0
O_2	11 + 1 x pH	240	--	1.6^4
H_2	9.6 + 1 x pH	13	$H_2O \rightarrow * H \overset{H_2O}{\rightarrow} H_2$	2
CO	20	38	$CO_2 \overset{H_2O}{\rightarrow} * C_1$	1
HCOO-	35	-104		
C2H4	58	-123	$2 \times \left(CO_2 \overset{H_2O}{\rightarrow} * CO\right)$	3
EtOH	63	-123	$* CO \overset{H_2O}{\rightarrow} * CHO$ $* CHO + * CO \rightarrow * C_2$	
PrOH	67	-135	$3 \times \left(CO_2 \overset{H_2O}{\rightarrow} * CO\right)$ $* CO \overset{H_2O}{\rightarrow} * CHO$ $* CHO + * CO \rightarrow * OCCHO$ $* OCCHO + * CO \rightarrow * C_3$	4

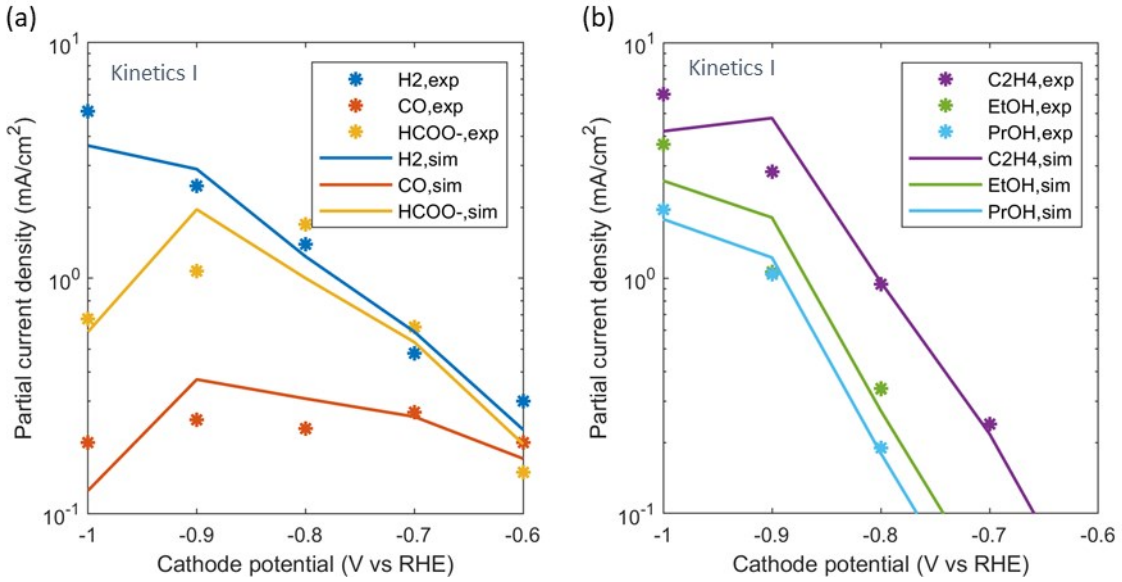

Figure S1 Comparison between the experimental partial current densities[1] and the simulated partial current densities using the extracted kinetic parameters after correcting for concentration polarization effects assuming an 80-μm boundary-layer thickness.

Additional model parameters

The binary gas-phase diffusion coefficients are estimated following derivation by Fuller *et al.*,[5]

$$D_{iq}[cm^2\ s^{-1}] = \frac{10^{-3}T[K]^{1.75}\left(M_i[g\ mol^{-1}]^{-1} + M_q[g\ mol^{-1}]^{-1}\right)^{0.5}}{p_G[atm]\left(v_{p,i}^{0.33} + v_{p,q}^{0.33}\right)^2} \quad \text{(S2)}$$

where $v_{p,i}$ is the diffusion volume of species i.

The diffusion coefficient of ionic species in the membrane/ionomer are back calculated from the membrane conductivity,

$$D_j = -\frac{\kappa_j^{eff,M} RT}{z_i F^2} \quad \text{(S3)}$$

The temperature-dependent transport and material properties of the membrane/ionomer are summarized in **Table S2**. The liquid-equilibrated properties and the electro-osmotic coefficient are assumed to be independent of temperature. The temperature dependence of the vapor-equilibrated membrane properties was assumed linear and their values were interpolated/extrapolated from values at 298 K and 350 K.

The overall effective EOC, $\xi_A^{eff,M}$, is derived from rearranging the equation for the electro-osmotic flux of water as follows,

$$N_w^{EO} = \sum_j \xi_j^{eff,M} N_j = \sum_j \frac{\xi_j^{eff,M}}{z_j} \cdot z_j N_j \quad \text{(S4)}$$

Since data for the ξ_j for each ionic species in an AEM is not complete, we make a simplifying assumption that ξ_j / z_j is the same for all species, and define an overall effective EOC as,

$$\xi_A^{eff,M} = -\frac{\xi_j^{eff,M}}{z_j} \quad \text{(S5)}$$

where the negative sign is to ensure a positive value of $\xi_A^{eff,M}$ since $z_j < 0$ for the main charge-carrying species in AEMs. Plugging equation (S5) into equation (S4) and rearranging gives,

$$N_w^{EO} = -\xi_A^{eff,M} \sum_j z_j N_j = -\xi_A^{eff,M} \frac{i_L}{F} \quad \text{(S6)}$$

Table S2 Membrane/ionomer properties[6-10]

Transport coefficient (mol²/J·cm·s)	α_V @ 298 K	$8.0 \times 10^{-14} \exp(11.47 a_0)$
	α_V @ 350 K	$2.3 \times 10^{-13} \exp(11.47 a_0)$
	α_L	$100 \alpha_V^{max}$
Water content	λ_V @ 298 K	$30.75 a_0^3 - 41.19 a_0^2 + 21.14 a_0$
	λ_V @ 350 K	$21.90 a_0^3 - 20.60 a_0^2 + 8.35 a_0$
	λ_L	17
Ion conductivity (S/m)	κ_V @ 298 K	$0.003 \exp(8.14 a_0)$
	κ_V @ 350 K	$0.006 \exp(6.21 a_0)$
	κ_L	$2\kappa_V$
Electro-osmotic coefficient	ξ_V	0.61
	ξ_L	3
CO_2 diffusivity (m²/s)	D_{CO_2}	$2.17 \times 10^{-9} \exp\left(-2345\left(\frac{1}{T[K]} - \frac{1}{303}\right)\right)$
CO_2 solubility (mM/atm)	H_{CO_2}	$34 \exp\left(-2400\left(\frac{1}{T[K]} - \frac{1}{298}\right)\right)$

Table S3 DM and CL properties[11-14]

Intrinsic porosity	ϵ_{DM}^o	0.526
	ϵ_{CL}^o	0.5
Ionomer volume fraction in pore space	$f_{I,DM}$	0
	$f_{I,CL}$	0.4
Electronic conductivity (S/m)	σ_{DM}	220
	σ_{CL}	100
Saturated Permeability (m²)	ψ_{DM}	8.4×10^{-13}
	ψ_{CL}	8.0×10^{-16}

The saturation curves used for the DMs, CLs, and membrane are shown in **Figure S2**. The saturation curves for the DM and CL are adopted from the experimental measurements reported by Zenyuk et al.[15] and the saturation curve for the membrane was adopted from the theoretical work of Weber et al. for a cation-exchange membrane.[16]

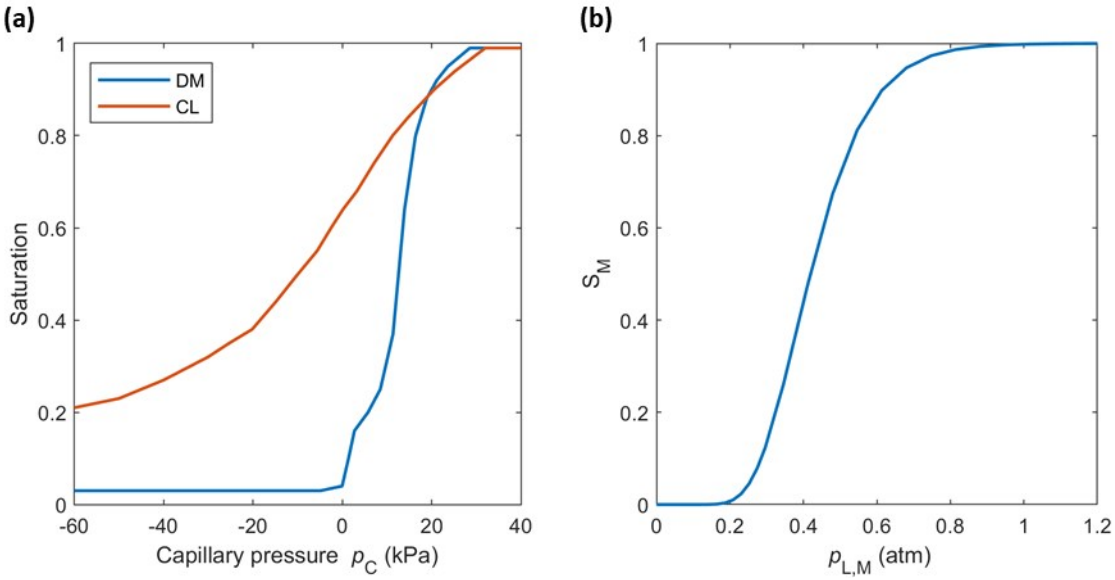

Figure S2 (a) Saturation curve for the DM and CL.[15] (b) Saturation curve to describe membrane hydration between vapor- and liquid-equilibrated states.[16]

Equations for applied-voltage breakdown (AVB)

Table S4 lists the equations used to determine each of the components in the applied voltage breakdown plots. U^o is the standard electrode potential. Since multiple reactions occur at the cathode, the standard cathode potential depends on FE of each reaction k such that $U_{cathode}^{o} = \sum_k FE_k U_k^o$. $i_{v,k}$ is the local current source in A/m^3, i_k in the local current density in A/m^2, $i_{o,k}$ is the exchange current density, $\alpha_{a/c,\,k}$ is the anodic/cathodic transfer coefficient, and η_k is the overpotential for reaction k. i_T is the total current density of the cell, and $i_{v,T} = \sum_k i_{v,k}$ is the total current source. κ^{eff} is the effective ionic conductivity of the ionomer in the CL and membrane.

Table S4 Equations for calculating the applied-voltage breakdown

Standard cell potential
$$U_{cell}^{o} = U_{anode}^{o} - U_{cathode}^{o} \quad \text{(S7)}$$
Kinetic overpotential
$$\eta_{kinetic} = \sum_k \frac{RT}{i_T \alpha_{a/c,k} F} \int_{CL} i_{v,k} \ln\left(\frac{i_k}{i_{o,k} \prod_j a_{o,j}^{\gamma_j}}\right) \quad \text{(S8)}$$
Mass transport overpotential
$$\eta_{mass\ transport} = \sum_k \frac{2.303RT}{i_T F} \int_{CL} i_{v,T}(pH_o - pH) + \frac{1}{i_T} \int_{CL} i_{v,k}\eta_k - \eta_{k,\,kinetic} \quad \text{(S9)}$$
Ohmic overpotential
$$\eta_{ohmic} = \frac{1}{i_T} \int_{CL+MEM} \frac{i^2}{\kappa^{eff}} \quad \text{(S10)}$$

Supplementary Figures

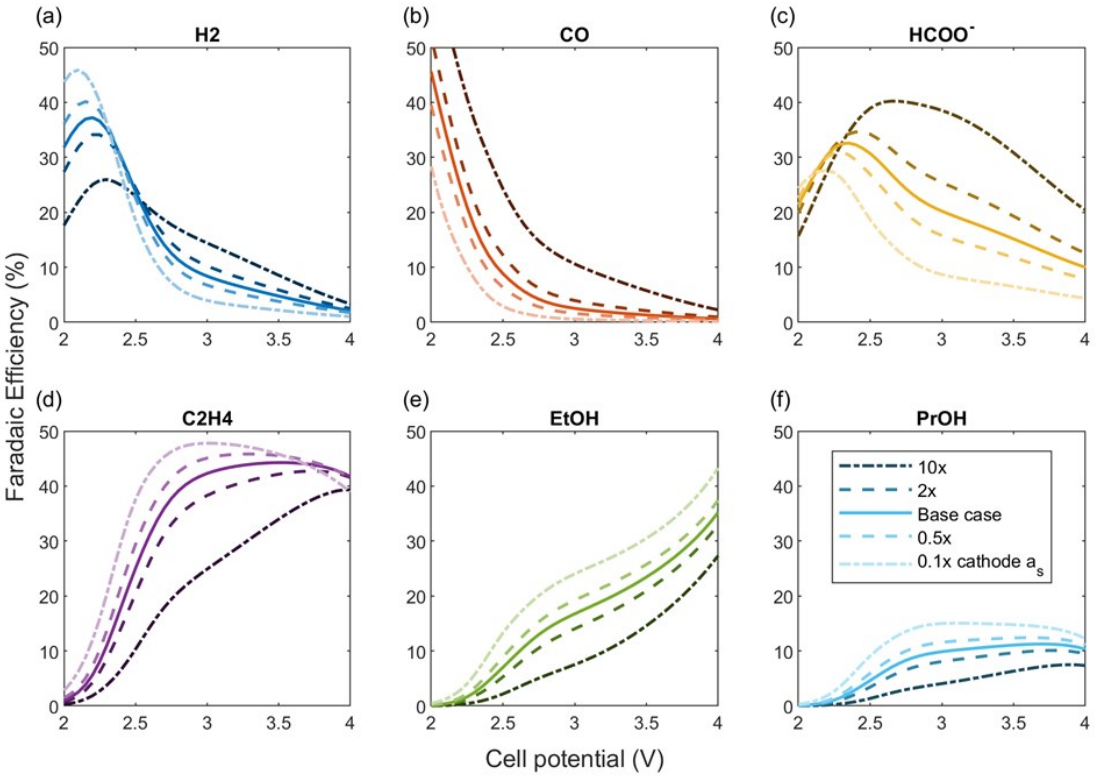

Figure S3 The faradaic efficiencies for the six cathode products for Cu-MEAs with varying cCL specific surface areas. Lighter shade represents a lower specific surface area. The effects of decreasing cCL specific surface area is similar to that of decreasing cCL thickness.

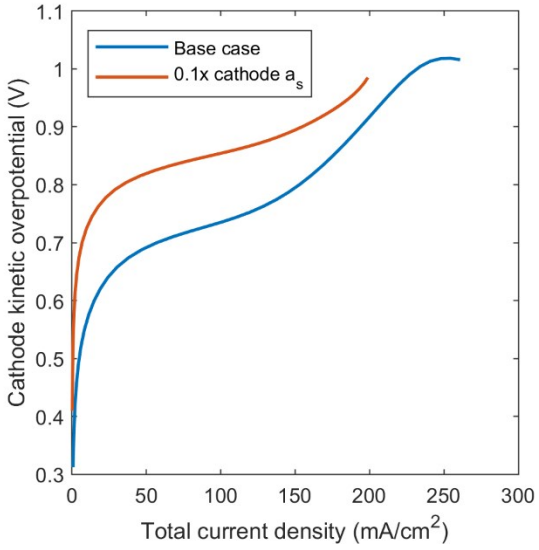

Figure S4 The cathode kinetic overpotential for the base case and the case with 0.1x cathode specific surface area. The lower active surface area requires a higher cathode overpotential to maintain the same total current density.

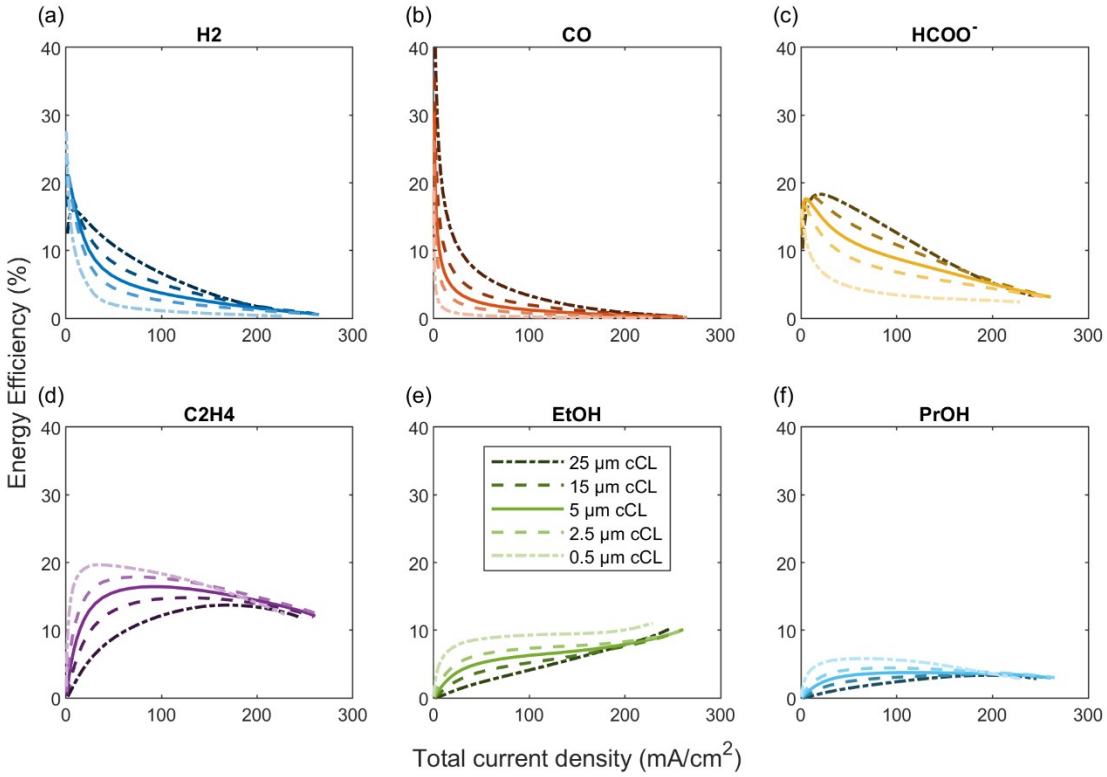

Figure S5 The energy efficiencies for the six cathode products for Cu-MEAs with a 25 μm, 5 μm, 2.5 μm, and 0.5 μm cCL. Lighter shade represents a thinner cCL. Decreasing the cCL thickness can increase the EE of C_2H_4, EtOH, and PrOH without sacrificing the total production rate.

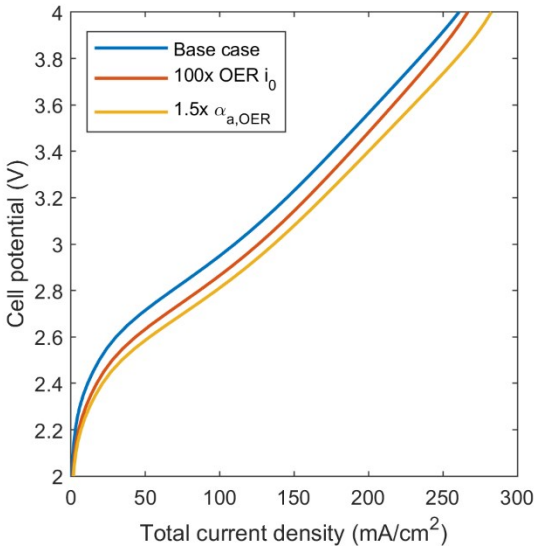

Figure S6 The polarization curves of Cu-MEAs using an anode catalyst with improved OER kinetics.

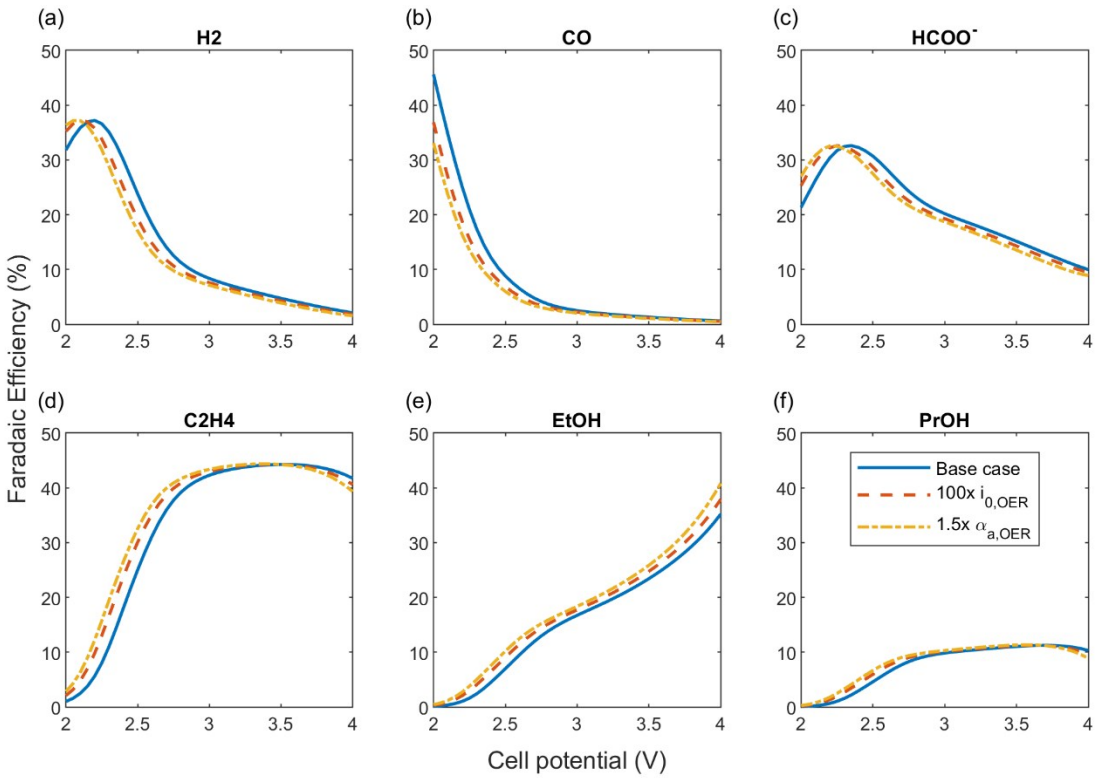

Figure S7 The faradaic efficiencies for the six cathode products for Cu-MEAs using an anode with improved OER kinetics.

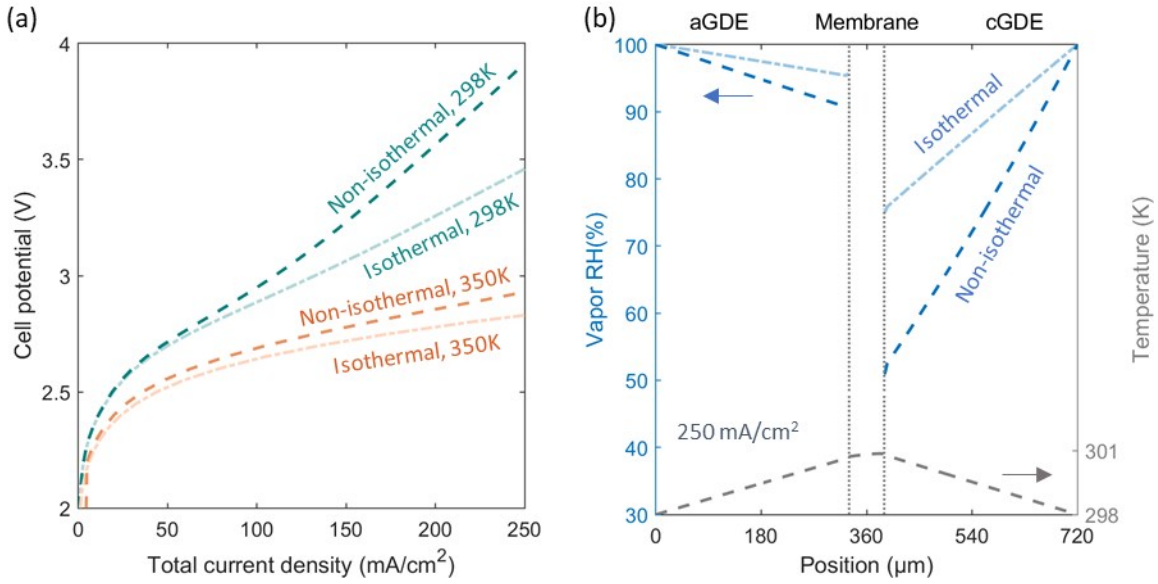

Figure S8 (a) Polarization curves at 298 K (teal) and 350 K (orange) simulated with an isothermal (lighter shade, dot-dash) and non-isothermal (dashed) model. (b) The vapor RH and temperature profile at 250 mA/cm^2. Heating due to inefficiencies raises the cell temperature and lowers the RH in the GDEs.

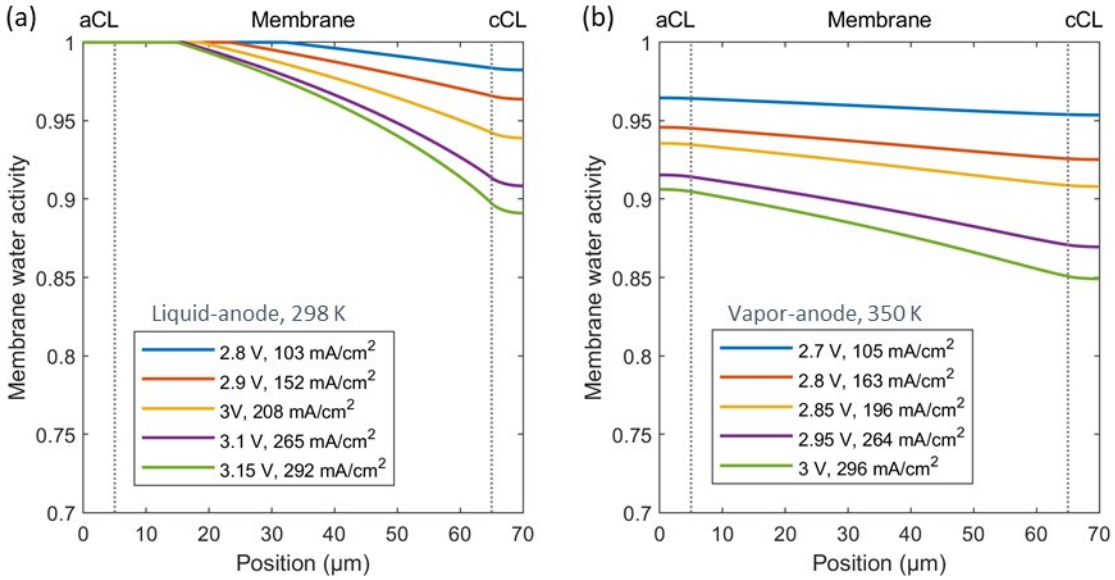

Figure S9 Membrane water activity profile for (a) liquid-fed anode at 298 K and (b) vapor-fed anode at 350 K.

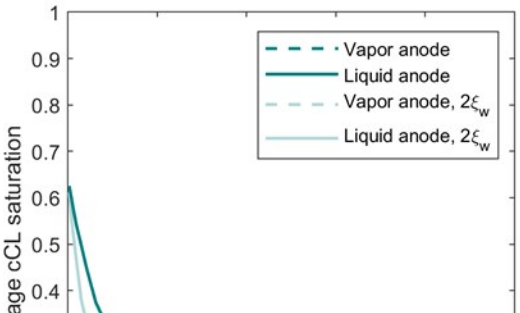

Figure S10 The average cCL saturation for vapor-water anode feed (dashed) and liquid-water anode feed (solid) Cu-MEAs at 298 K. Lighter shade represents simulation with 2x EOC.

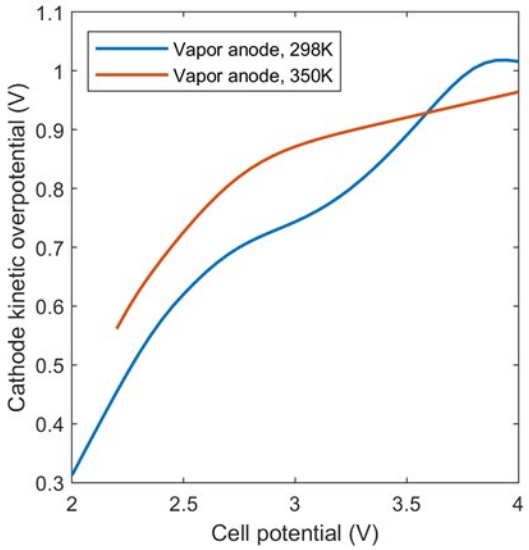

Figure S11 The cathode kinetic overpotential at 298 K (blue) and 350 K (orange) for the vapor-fed Cu-MEA. The overpotentials are redistributed due to changes in cell properties.

Rate parameters and simulations for alternate kinetics

As noted in the text, a second set of self-consistent rate equations was used to assess the impacts of the MEA architecture. The same process of fitting the equations was used as detailed above to obtain the rate parameters for a second set of self-consistent kinetics,[3, 17] summarized in **Table S5**. We used two Tafel equations to better fit the H_2 partial current density empirically. The pH dependence for CH_4 was estimated based on the trend observed by Wang et al.[3] **Figure S12** shows how the simulated partial current densities for the aqueous system compare to experimental data.

Table S5 Rate parameters obtained from measurements by reference 5 (Kinetics II)

	U_k^o (V)	$i_{o,k}$ (mA cm^{-2})	$\alpha_{a/c,k}$	$\prod_j a_j^{\gamma_{j,k}}$	**Ref.**
HER & CO_2R on polished Cu foil					3, 17
H_2 (η < -0.8 V)	0	$2.2 \times 10^{-8} \exp\left(-\frac{0.01[eV]pH}{k_BT}\right)$	0.69	a_w^2	
H_2 (η > -0.8 V)		$1.7 \exp\left(-\frac{0.01[eV]pH}{k_BT}\right)$	0.12	a_w^2	
CO	-0.11	1.1×10^{-4}	0.10	$a_w\left(\frac{[CO_2]}{1\ M}\right)^{1.50}$	
$HCOO^-$	-0.02	5.4×10^{-7}	0.24	$a_w\left(\frac{[CO_2]}{1\ M}\right)^{2.00}$	
C_2H_4	0.07	3.4×10^{-13}	0.69	$a_w^3\left(\frac{[CO_2]}{1\ M}\right)^{1.36}$	
C_2H_5OH	0.08	1.4×10^{-19}	1.10	$a_w^3\left(\frac{[CO_2]}{1\ M}\right)^{0.96}$	
CH_4	0.17	$8.5 \times 10^{-18} \exp\left(-\frac{0.02[eV]pH}{k_BT}\right)$	1.13	$a_w\left(\frac{[CO_2]}{1\ M}\right)^{0.84}$	

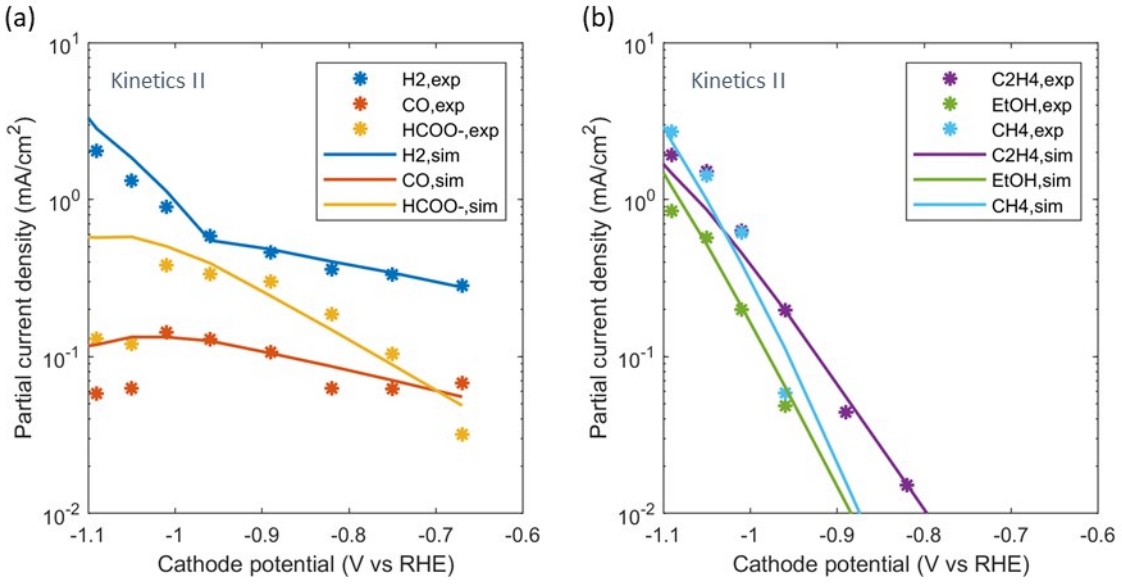

Figure S12 Comparison between the experimental partial current densities[17] and the simulated partial current densities using the extracted kinetic parameters after correcting for concentration polarization effects assuming an 80-µm boundary-layer thickness.

References

1. M. Ebaid, K. Jiang, Z. Zhang, W. S. Drisdell, A. T. Bell and J. K. Cooper, *Chem. Mater.*, 2020, DOI: 10.1021/acs.chemmater.0c00761.
2. E. L. Clark, J. Resasco, A. Landers, J. Lin, L.-T. Chung, A. Walton, C. Hahn, T. F. Jaramillo and A. T. Bell, *ACS Catal.*, 2018, DOI: 10.1021/acscatal.8b01340, 6560-6570.
3. L. Wang, S. A. Nitopi, E. Bertheussen, M. Orazov, C. G. Morales-Guio, X. Liu, D. C. Higgins, K. Chan, J. K. Nørskov, C. Hahn and T. F. Jaramillo, *ACS Catal.*, 2018, **8**, 7445-7454.
4. T. Schuler, T. Kimura, T. J. Schmidt and F. N. Büchi, *Energy Environ. Sci.*, 2020, DOI: 10.1039/D0EE00673D.
5. E. N. Fuller, P. D. Schettle and J. C. Giddings, *Ind. Eng. Chem.*, 1966, **58**, 19-+.
6. Y. S. Li, T. S. Zhao and W. W. Yang, *Int. J. Hydrogen Energy*, 2010, **35**, 5656-5665.
7. J. Peng, A. L. Roy, S. G. Greenbaum and T. A. Zawodzinski, *J. Power Sources*, 2018, **380**, 64-75.
8. M. Adachi, T. Navessin, Z. Xie, F. H. Li, S. Tanaka and S. Holdcroft, *J. Membrane Sci.*, 2010, **364**, 183-193.
9. Z. C. Liu, H. Z. Yang, R. Kutz and R. I. Masel, *J. Electrochem. Soc.*, 2018, **165**, J3371-J3377.
10. X. H. Wang, J. P. McClure and P. S. Fedkiw, *Electrochim. Acta*, 2012, **79**, 126-132.
11. N. Khajeh-Hosseini-Dalasm, M. J. Kermani, D. G. Moghaddam and J. M. Stockie, *Int. J. Hydrogen Energy*, 2010, **35**, 2417-2427.
12. C. Y. Du, P. F. Shi, X. Q. Cheng and G. P. Yin, *Electrochem. Commun.*, 2004, **6**, 435-440.
13. A. El-Kharouf, T. J. Mason, D. J. L. Brett and B. G. Pollet, *J. Power Sources*, 2012, **218**, 393-404.
14. I. V. Zenyuk, E. Medici, J. Allen and A. Z. Weber, *Int. J. Hydrogen Energy*, 2015, **40**, 16831-16845.
15. I. V. Zenyuk, P. K. Das and A. Z. Weber, *J. Electrochem. Soc.*, 2016, **163**, F691-F703.
16. A. Z. Weber, R. M. Darling and J. Newman, *J. Electrochem. Soc.*, 2004, **151**, A1715-A1727.
17. K. P. Kuhl, E. R. Cave, D. N. Abram and T. F. Jaramillo, *Energy Environ. Sci.*, 2012, **5**, 7050-7059.